Published in final edited form as:

Adv Funct Mater. 2020 February 26; 30(9): . doi:10.1002/adfm.201908825.

Gold Nanoframeworks with Mesopores for Raman–Photoacoustic Imaging and Photo-Chemo Tumor Therapy in the Second Near-Infrared Biowindow

Jinping Wang

Department of Biomedical Engineering, Stevens Institute of Technology, Hoboken, NJ 07030, USA

Jingyu Sun

Department of Chemistry and Chemical Biology, Stevens Institute of Technology, Hoboken, NJ 07030, USA

Yuhao Wang

Department of Biomedical Engineering, Stevens Institute of Technology, Hoboken, NJ 07030, USA

Tsengming Chou

Laboratory for Multiscale Imaging, Stevens Institute of Technology, Hoboken, NJ 07030, USA

Qiang Zhang

Department of Biomaterials, Key Laboratory of Biomedical Engineering of Fujian Province, State Key Lab of Physical Chemistry of Solid Surface, College of Materials, Xiamen University, Xiamen, Fujian 361005, P. R. China

Beilu Zhang

Department of Chemistry and Chemical Biology, Stevens Institute of Technology, Hoboken, NJ 07030, USA

Lei Ren

Department of Biomaterials, Key Laboratory of Biomedical Engineering of Fujian Province, State Key Lab of Physical Chemistry of Solid Surface, College of Materials, Xiamen University, Xiamen, Fujian 361005, P. R. China

Hongjun Wang

Department of Biomedical Engineering, Stevens Institute of Technology, Hoboken, NJ 07030, USA

Department of Chemistry and Chemical Biology, Stevens Institute of Technology, Hoboken, NJ 07030, USA

Prof. H. Wang, hongjun.wang@stevens.edu, Prof. L. Ren, renlei@xmu.edu.cn.

The ORCID identification number(s) for the author(s) of this article can be found under https://doi.org/10.1002/adfm.201908825.

Supporting Information

Supporting Information is available from the Wiley Online Library or from the author.

Conflict of Interest

The authors declare no conflict of interest.

Abstract

Gold-based nanostructures with tunable wavelength of localized surface plasmon resonance (LSPR) in the second near-infrared (NIR-II) biowindow receive increasing attention in phototheranostics. In view of limited progress on NIR-II gold nanostructures, a particular liposome template-guided route is explored to synthesize novel gold nanoframeworks (AuNFs) with large mesopores (≈40 nm) for multimodal imaging along with therapeutic robustness. The synthesized AuNFs exhibit strong absorbance in NIR-II region, affording their capacity of NIR-II photothermal therapy (PTT) and photoacoustic (PA) imaging for deep tumors. Functionalization of AuNFs with hyaluronic acid (HA) endows the targeting capacity for CD44-overexpressed tumor cells while gatekeeping doxorubicin (DOX) loaded into mesopores. Conjugation of Raman reporter 4-aminothiophenol (4-ATP) onto AuNFs yields a surface-enhanced Raman scattering (SERS) fingerprint for Raman spectroscopy/imaging. In vivo evaluation of HA-4-ATP-AuNFs-DOX on tumor-bearing xenografts demonstrates its high efficacy in eradication of solid tumors in NIR-II under PA–Raman dual image-guided photo-chemotherapy. Thus, current AuNFs offer versatile capabilities for phototheranostics.

Keywords

chemotherapy; gold nanoframeworks; photoacoustic imaging; Raman imaging; second near-infrared photothermal therapy

1. Introduction

Phototheranostics, light-enabled concomitant diagnosis and therapy, emerges as a promising strategy to treat cancer with recognized advantages such as minimal invasiveness, high efficacy and specificity, and spatiotemporally controlled release of therapeutics.[1] Combination with nanostructures to achieve near-infrared (NIR) light-mediated phototheranostics becomes even more compelling for the possibility of improving treatment depth.[2] In this regard, gold-based nanomaterials have received particular attention for their tunable wavelength of localized surface plasmon resonance (LSPR) from visible to NIR regions, in conjunction with versatile chemical modification and high biocompatibility,[3] leading to applications in sensing,[4] photoacoustic (PA) imaging,[5] drug delivery,[6] photothermal therapy (PTT),[7] and photodynamic therapy.[2b]

In view of deeper tissue penetration (>2 cm vs ≈1 cm) and higher maximum permissible exposure (MPE) (1 W cm^{-2} vs 0.33 W cm^{-2} in skin, American National Standard for Safe Use of Lasers, ANSI Z136.1–2007) with the second NIR biowindow (NIR-II: 1000–1350 nm) compared to the first (NIR-I: 750–1000 nm),[8] it is highly desirable for gold nanomaterials to have NIR-II LSPR. As a matter of fact, various nanomaterials such as copper sulfide nanoparticles,[9] carbon-based nanomaterials,[10] Mxene,[11] and polypyrrole nanostructures[12] have been explored for PTT and in vivo photo -acoustic tomography (PAT) in NIR-II region. So far, limited progress has been made to gold nanostructures. Furthermore, even some nanomaterials such as MXene@Gold nanocomposites can achieve PTT effects in NIR-II but they still retain their PAT capacity in NIR-I (around 900 nm) due to relatively low NIR-II absorbance.[2c] To this end, exploration of gold-based

phototheranostic agents highly active in NIR-II can hold great potentials for high penetration depth PTT and PAT in antitumor therapy.

The intense electromagnetic field in the vicinity of gold nanostructures from their LSPR can enable surface-enhanced Raman scattering (SERS) for bioanalysis.[13] In particular, SERS-based Raman imaging offers the opportunity to detect tumors with high specificity and sensitivity.[14] Based on the “fingerprint” scattering signals of reporter molecules, SERS-based Raman imaging can sensitively track reporter molecule-linked gold nanotherapeutics in tumors and therefore specifically distinguish the reporter molecule-containing tumors from surrounding normal tissues.[15] When coupled with NIR-II PAT, SERS-based Raman imaging can delineate malignant tissues at a high spatial resolution (several micrometers) while achieving deep observation (several centimeters) of a local solid tumor via NIR-II PAT.[16] Thus, development of well-structured gold nanotherapeutics highly active in the NIR-II region is of great importance for PAT–Raman bi-modal imaging-guided photothermal therapy of cancer.

To obtain highly active NIR-II gold nanotherapeutics, a new nanostructure, a gold nanoframework (AuNF) with large mesopores (≈40 nm), was facilely synthesized via a simple and green approach, and such AuNFs showed strong absorbance in the NIR-II biowindow for PTT and exhibited potential for PAT and SERS-based Raman imaging (Scheme 1a,b). To guide the formation of AuNFs, biocompatible liposomes were used as templates, which effectively circumvented hard-to-remove and cytotoxic reagents such as cetyltrimethyl ammonium bromide (CTAB),[17] oleylamine,[18] and sodium borohydride,[19] commonly used in preparation of gold nanostructures. The large cavities of mesopores in AuNFs enabled encapsulation of small-molecule cargos such as chemotherapeutics for local delivery. Doxorubicin (DOX), an ideal model drug for its broad anticancer activity and relatively stable fluorescence for in vitro and in vivo tracking,[20] was chosen to evaluate the drug-loading efficiency of AuNFs. Through thiol (−SH) groups, a Raman reporter, 4-aminothiophenol (4-ATP), was linked onto the surface of AuNFs. Hyaluronic acid (HA), a natural polysaccharide with high affinity for CD44,[20] was further grafted onto the surface of AuNFs to obtain an HA-4-ATP-AuNFs-DOX nanosystem via the formation of amide bonds between carboxylic groups of HA and amino groups of 4-ATP. In this nanosystem, the grafted HA not only acted as the cap for trapped DOX within mesopores but also endowed AuNFs with stability, biocompatibility, CD44-overexpressing tumor target ability, and functional groups for Raman reporter-linking. In vitro and in vivo performance of HA-4-ATP-AuNFs-DOX nanosystems, including cell uptake and cytotoxicity, ability to target cancer cells, NIR-II PTT, NIR-II PAT and Raman imaging capability, tumor therapeutic ability, and biosafety assessment, were systematically investigated. As recognized, HA-4-ATP-AuNFs-DOX nanosystems exhibited several unique features, such as 1) high biocompatibility from liposome-directed synthesis of AuNFs without the use of any toxic reagents, 2) strong absorbance and high photothermal conversion efficiency in NIR-II for PTT tumor treatment, 3) potential to load a high quantity of anticancer drugs in the mesoporous cavities of AuNFs for chemotherapy, 4) targeted accumulation in tumors for NIR-II-enabled tumor specific PTT and chemotherapy, and 5) the capability of identifying biodistribution and guiding PTT/chemotreatment using in vivo bimodal PAT and Raman imaging in NIR-II. HA-4-ATP-AuNFs-DOX nanosystems are therapeutically effective in

eliminating solid tumors with NIRII-enabled PTT/chemotherapy. Taken together, this study not only promotes the development of gold based nanomaterials for NIR-II PTT tumor treatment, but also provides guidelines to design other nanosystems for PAT and SERS-based Raman imaging.

2. Results and Discussion

2.1. Synthesis and Characterization of HA-4-ATP-AuNFs-DOX Nanosystems

To fabricate porous gold nanostructures with NIR-II LSPR, a new synthesis approach was developed by using liposomes as a template, under the reduction of ascorbic acid (AA) as reported previously.[21] Liposomes were prepared from 1,2-dipalmitoyl-*sn*-glycero-3-phosphocholine (DPPC) and cholesterol following the established thin-film hydration method.[22] During the process, thin lipid films were hydrated with a high concentration (300×10^{-3} M) of AA aqueous solution. Previous report suggests that the pH of hydration solution can influence the size of liposomes.[23] In this study, at low pH (5.09) caused by the high concentration of AA (300×10^{-3} M), the synthesized liposomes had a relatively small size of 44.5 ± 2.2 nm as determined by the nanosizer (Figure S1a, Supporting Information) and appeared spherical (Figure S1b, Supporting Information).

AA in the liposome solution can act as the reducing agent to reduce $HAuCl_4$ into Au.[24] With a constant amount of liposomes, AuNFs could be generated by gradually increasing the concentration of $HAuCl_4$. As shown in Figure S2 (Supporting Information), at low concentrations of $HAuCl_4$ (e.g., 1×10^{-3} M), small Au nanostructures were formed (Figure S2a, Supporting Information). Scanning electron microscope (SEM) examination of such structures revealed the presence of mesopores among Au frameworks, and the size of mesopores was similar to that of liposomes (Figure S2b, Supporting Information). When the concentration of $HAuCl_4$ increased to 3×10^{-3} M, the interconnected mesopores began to form complex 3D architecture. Beyond this concentration, no significant change in morphology and mesopore structure was identified except for increase of AuNF size. As a matter of fact, both average mesopore size and thickness of Au frameworks from all investigated $HAuCl_4$ concentrations were comparable (Table S1, Supporting Information). With 8×10^{-3} M $HAuCl_4$, well-dispersed porous AuNFs with uniform shape and size (Figure 1b) were successfully generated via liposome templates as illustrated in Figure 1a. Dynamic light scattering indicates the mean hydrodynamic diameter of AuNFs as 140.2 ± 3.2 nm (Figure S3, Supporting Information). SEM examination of these AuNFs further revealed that the well-defined mesoporous structures distributed throughout the entire outer surface of AuNFs (Figure 1c). Further inspection of 3D electron tomography of AuNFs reconstructed from tilted series (Figure 1d; Video S1, Supporting Information) confirms that the mesopores are also distributed throughout the interior of AuNFs, and they are interconnected to form a bicontinuous structure. The presence of uneven peaks in selected Au element line scanning (Figure S4, Supporting Information) also confirmed the cratered mesopores of AuNFs. As determined by high-resolution transmission electron microscope (HRTEM) and corresponding electron diffractions (Figure 1e–g), such AuNFs are polycrystalline. The selected-area electron diffraction (SAED) patterns of single AuNF (Figure 1g) show concentric rings of spots, which are indexed to a face-centered cubic (fcc) crystal

structure[25] and indicate random aggregation of multiple Au nanocrystals to form nanoframeworks, rather than oriented growth. In addition, the progress of AuNF development could also be visually monitored via color change of the reaction solution. Typically, the reaction solution started as milk white and progressively turned to light blue and blue gray as $AuCl_4^-$ was converted into optically lossy Au. The color of final AuNF solutions was greatly dependent on the initial concentration of $HAuCl_4$ (Figure S5, Supporting Information). Parallel experiments were also performed to affirm the necessity of liposome templates in AuNF formation. Indeed, in the absence of liposomes, only solid Au nanoparticles were formed (Figure S6a, Supporting Information). Based on current findings, we believe that AuNFs grow around spherical liposomes via possible electrostatic interaction between $AuCl_4^-$ and the $-N(CH_3)_3^+$ of DPPC[26] and with increasing $HAuCl_4$ brings more liposomes together to form aggregated liposome networks and subsequently guides the formation of 3D AuNFs within the interliposome space with liposomes defining the mesopores.

As evidenced from previous reports,[27] plasmonic metal nanoparticles containing additional nanoscale pores exhibit notable redshift in LSPR wavelength compared to smooth ones. In this regard, it is reasonable to postulate that with the increase of mesopores and size of AuNFs, redshift of the LSPR wavelength may occur following the illustration in Figure S2c (Supporting Information). To demonstrate this, UV–vis–NIR spectra of AuNFs prepared from various $HAuCl_4$ concentrations were obtained. As expected, the peak resonance absorbance band shifted from 750 to 1150 nm as $HAuCl_4$ concentration increased from 1×10^{-3} to 8×10^{-3} M (Figure 2a), which was significantly different from that of Au nanoparticles prepared without liposomes (650 nm) (Figure S6b, Supporting Information). It is necessary to mention that AuNFs aqueous solutions made with 8×10^{-3} M $HAuCl_4$ have a very strong absorbance peak in the NIR-II biowindow, in contrast to limited absorbance of other reported NIR-II photothermal nanoagents like B–TiO_{2-x} nanoparticles,[8c] Au plasmonic blackbodies,[28] and Nb_2C@$mSiO_2$ nanomaterials.[8a] In view of the limited development of photothermal nanoagents active in the NIR-II region (much higher tissue penetration than NIR-I), such AuNFs can serve as new efficient photothermal-conversion nanoagents for PTT in the NIR-II biowindow (1064 nm in this study). As demonstrated in Figure 2b,e, AuNF aqueous solutions at various concentrations were continuously irradiated with a 1064 nm laser for 6 min. The temperature elevation is closely related to irradiation time and AuNFs' concentration. The temperature of AuNFs' dispersion at a concentration of 200 μg mL^{-1} raised from 25.0 to 52.5 °C after 6 min of irradiation, which is high enough to kill cancer cells via hyperthermia.[29] The photothermal-conversion efficiency of AuNFs under 1064 nm laser irradiation was calculated to be 23.9% based on Figure 2c,d. Following the Beer's law ($A/L = \alpha C$, where α is the extinction coefficient), a linear dependence of A/L on the concentration was obtained (Figure S7, Supporting Information), and the extinction coefficient at 1064 nm was measured to be 26.2 L g^{-1} cm^{-1}, which was significantly higher than that of gold nanorods (3.9 L g^{-1} cm^{-1}).[30] We also assessed the photothermal stability and reliability by recording the temperature profiles of AuNF solutions during four cycles of the heating and cooling process with 1064 nm laser irradiation (Figure S8, Supporting Information). No significant attenuation was observed for each cycle, suggesting the potential of AuNFs as highly reliable photothermal agents for cancer treatment.

Given the strong absorbance of AuNFs in NIR-II, their PAT effect was assessed by a PA imaging system. As shown in Figure S9 (Supporting Information), AuNFs generated a strong PA signal in the NIR-II region (about 1200 nm), which is consistent with its absorption spectrum (Figure 2a). Obviously, AuNFs could induce intense optoacoustic signals at the 1200 nm wavelength (Figure 2f). Furthermore, the PA signal intensity exhibited a linear response to AuNF concentration (Figure 2g), demonstrating the possibility of AuNFs as NIR-II PA contrast agents for imaging-guided cancer theranostics.

Additionally, AuNFs have the potential to be used for SERS-based Raman imaging considering the possible presence of “hotspots,” where the resonated electromagnetic field significantly amplifies Raman scattering of target molecules.[31] Actually, the sensitivity of SERS-based Raman imaging greatly depends on “hotspots” of Au nanoparticles, which can come from rough surface,[32] sharp tips,[33] and inter- or intraparticle nanogaps.[34] Both mesopores and frameworks of AuNFs can lead to the formation of electromagnetic “hotspots.” To confirm the formation of hotspots within AuNFs, distribution of a near-field electromagnetic field was simulated by finite-difference time domain (FDTD) (Figure 2h). Interestingly, within individual AuNFs the small gaps between mesopores act as resonators to significantly enhance the intensity of local electromagnetic fields even more than mesopores themselves, indicating a high density of hotspots in AuNFs for possible SERS analysis. In that regard, a representative Raman reporter, 4-ATP, was conjugated onto the surface of AuNFs via stable Au–S bonds.[35] SERS capability of AuNFs in detecting immobilized 4-ATP-containing molecules was evidently confirmed by the obtained Raman spectra as shown in Figure 3a, in which AuNFs alone, 4-ATP alone, and HA-4-ATP-AuNFs at the same concentration were investigated. Compared to 4-ATP alone, HA-4-ATP-AuNFs showed noticeably enhanced Raman signals, which can be readily attributed to the adsorption of 4-ATP-containing molecules onto mesopore surface close to the “hotspots” of AuNFs.

To render AuNFs with targeting specificity, HA, the most specific ligand for CD44, which is typically overexpressed in metastatic cancer cells,[36] were first reacted with Raman reporter 4-ATP via 1-ethyl-3-(3-dimethyllaminopropyl) carbodiimide hydrochloride (EDC)-enabled crosslinking of amino groups in 4-ATP with carboxylic groups in HA, and then immobilized onto AuNFs via the high affinity between Au and thiols. Successful formation of HA-4-ATP-AuNFs was confirmed by Fourier transform infrared spectroscopy (FTIR) and zeta potential characterizations, respectively. As shown in Figure S10a (Supporting Information), characteristic bands of pure HA were consistently seen with HA-4-ATP-AuNFs, affirming the presence of HA in HA-4-ATP-AuNFs. Zeta potential of AuNFs alone was slightly negative (−7.6 mV) but HA-4-ATP-AuNFs became pronouncedly more negative (−24.7 mV) (Figure S10b, Supporting Information), indicating successful immobilization of HA-containing molecules onto AuNFs. The highly negative and hydrophilic HA can serve as a stabilizer for nanoparticles;[37] thus, high colloidal stability is expected with HA-4-ATP-AuNFs as well. As illustrated in Figure S11a (Supporting Information), nude AuNFs aggregated in water and precipitated on the bottom of the container after 7 days, whereas HA-4-ATP-AuNFs remained stable and without any noted size changes (Table S2, Supporting Information) for the entire investigating period. More importantly, HA-4-ATP-

AuNFs were well dispersed with excellent stability even in cell culture media (Figure S11b, Supporting Information), essential for further application in biological systems.

The mesopores in AuNFs can offer more surfaces and void space to accommodate biomolecules; as such HA-4-ATP-AuNFs could be ideal vehicles for drug delivery. Meanwhile, the long chain of HA could also act as gatekeeper to keep drug molecules inside the AuNFs. Under NIR-II laser irradiation, the photothermal effect of AuNFs can loosen the structure of the HA layer and decrease the viscosity of HA,[38] thereby enabling the release of cargo molecules. Taking advantage of the therapeutic endeavor to reduce tumorous HA by introduction of exogenous hyaluronidase-1 (Hyal-1),[39] Hyal-1-triggerred release of cargos from HA-coated AuNFs can be another appealing strategy. To evaluate the drug-loading capacity of AuNFs, HA-functionalized AuNFs were incubated with various concentrations of DOX to load the anticancer drug. After removal of excessive free DOX by centrifugal filtration, UV–vis–NIR spectra of DOX-loaded AuNFs were recorded to determine drug-loading ratio on these nanoframeworks (Figure 3b). It was found that the loading capacity of DOX in AuNFs increased as a function of drug concentrations (Figure S12, Supporting Information). The highest drug-loading ratio (weight ratio between DOX and AuNFs) at our tested conditions was determined to be ≈373.0 ± 24.5%, noticeably higher than other DOX-loaded nanostructures such as nanoshells,[40] nanosheets,[41] and mesoporous nanomaterials.[42] It is worth noting that the absorption of AuNFs in the whole NIR region was not affected by the DOX loading (Figure S13, Supporting Information). After successful loading of DOX into AuNFs, NIR-II light- or Hyal-1-triggered DOX release from HA-4-ATP-AuNFs was spectrometrically measured. As shown in Figure 3c, weak drug release was observed in solutions without Hyal-1 or laser irradiation, indicating the efficiency of HA on AuNF surface for retention of DOX within the mesopores. Upon addition of Hyal-1 and/or laser irradiation, rapid release of DOX from AuNFs was observed, which could be ascribed to the degradation of HA by Hyal-1 or thermal-induced collapse of HA.

All the above results demonstrated that HA-4-ATP-AuNFs could achieve high photothermal efficiency in NIR-II and could be tailored for tumor environment-triggered drug delivery.

2.2. Cellular Uptake of HA-4-ATP-AuNFs-DOX Nanosystems

To demonstrate the targeting specificity and on-demand intracellular release of DOX in tumor cells as illustrated in Figure 3d, HA-4-ATP-AuNFs-DOX nanostructures were, respectively, incubated with breast cancer cells (MBA-MD-231) or normal human umbilical vein endothelial cells (HUVECs), and then examined under a fluorescent microscope. It is expected that MBA-MD-231 cells with high expression of membranous CD44[43] can facilitate the binding of HA-4-ATPAuNFs-DOX and subsequent internalization via CD44 and clathrin dual-mediated endocytosis.[44] Indeed, strong red fluorescence (from DOX of HA-4-ATP-AuNFs-DOX) was observed with MDA-MB-231 cells ($CD44^+$), in contrast to significantly low fluorescence with HUVECs ($CD44^-$) (Figure 3e). Pretreatment of MDA-MB-231 cells with excessive free HA to block CD44 prior to incubation with HA-4-ATP-AuNFs-DOX led to a significant reduction of fluorescence signals, confirming the participation of CD44 in cellular uptake of DOX-loaded AuNFs. As quantified using ImageJ, the fluorescence intensity of HA-4-ATP-AuNFs-DOX-treated group was ≈3.6 times

higher than that of HA-blocked group (Figure S14, Supporting Information). To further track the intracellular distribution of ingested HA-4-ATP-AuNFs within MDA-MB-231 cells, ultrathin sections of cell pellet specimens were examined under TEM. A majority of HA-4-ATP-AuNFs was found in cytosolic vesicles (Figure 3f). From these results, we demonstrated that uptake of HA-4-ATP-AuNFs into MDA-MB-231 cells was primarily driven by active interactions between HA and CD44 on the cell membrane. Next, the photothermally induced intracellular release of drug molecules from AuNFs was determined by incubating MBA-MD-231 cells with HA-4-ATP-AuNFs-DOX for 2 h and then irradiating with a 1064 nm laser for 5 min. As shown in Figure S15 (Supporting Information), cells incubated with DOX-loaded HA-4-ATP-AuNFs without laser irradiation displayed relatively weak DOX fluorescence. In contrast, strong red fluorescence of DOX was observed in the nuclei after NIR-II laser irradiation at 1 W cm^{-2} for 5 min, indicating the light-enabled, on-demand release characteristics of internalized HA-4-ATP-AuNFs-DOX.

2.3. In Vitro SERS-Based Raman Imaging and Cell-Killing Effect of HA-4-ATP-AuNFs-DOX Nanosystems

To evaluate the capability of HA-4-ATP-AuNFs for cell-based SERS Raman imaging, MDA-MB-231 cells incubated with HA-4-ATP-AuNFs for 4 h were examined under a confocal Raman microscope. Similar to fluorescence imaging results (Figure 3e), SERS Raman imaging also confirmed extensive internationalization of HA-4-ATP-AuNFs based on strong Raman signals from HA-4-ATP-AuNFs and clear cell boundaries (Figure 4a). Raman spectra of two representative positions, i.e., outside (position I) and inside (position II) the cell, are shown in Figure 4b. Raman spectra obtained from position II showed pronounced Raman “fingerprint” bands of 4-ATP at 1085 and 1585 cm^{-1}, which were not seen in the Raman spectra of position I. Thus, HA-4-ATP-AuNFs could serve as a strong SERS contrast agent for image-guided cancer therapy.

To assure their further utility as a new theranostic agent, cytocompatibility of HA-4-ATP-AuNFs was determined with two representative cell types (HUVECs and MDA-MB-231 cells) by 3-(4,5-dimethyl-2-thiazolyl)-2,5-diphenyl-2*H*-tetrazolium bromide (MTT) assay after 24 h incubation with HA-4-ATP-AuNFs at various concentrations. Both cells maintained high cell viability (>95%), even with concentrations as high as 200 μg mL^{-1} (Figure S16, Supporting Information), indicating negligible cytotoxicity of HA-4-ATP-AuNFs at the tested concentrations.

Chemo-phototherapy, i.e., the combination of chemotherapy and phototherapy, emerges as a more effective strategy than monotherapy in tumor treatment.[45] Cell-killing efficiency of DOX-loaded HA-4-ATP-AuNFs to MDA-MB-231 cells under NIR-II light induction was assessed by MTT assay. MDA-MB-231 cells treated with DOX-loaded HA-4-ATP-AuNFs plus 1064 nm laser irradiation showed the lowest viability (6.2%), significantly lower than cells treated with HA-4-ATP-AuNFs plus 1064 nm laser irradiation (49.2%) or free DOX alone (40.6% @ 40 μg mL^{-1}) (Figure 4c; Figure S17, Supporting Information). Clearly, the high cell-killing capacity is from the synergistic effect of chemotherapy (DOX) and photothermal therapy (AuNFs). To better quantify the synergistic effect, the combination index (CI) was introduced,[46] where CI < 1, CI = 1, or CI > 1 denoted the synergism,

additivity, or antagonism, respectively. Based on the MTT result, the CI was calculated to be 0.625. Hence, we can conclude that PTT and chemotherapy reported here exhibited a synergistic antitumoral effect.

To further verify cell ablation effects of HA-4-ATP-AuNFs-DOX in conjunction with 1064 nm laser irradiation, MDA-MB-231 cells treated with different conditions were stained with a calcein acetoxymethyl ester (Calcein-AM) and propidium iodide (PI) to visualize live and dead cells (Figure 4d). In contrast to very limited or no red fluorescence (PI for dead cells) with cells treated with phosphate buffer solution (PBS) or HA-4-ATP-AuNFs, a dramatically elevated number of red fluorescently stained cells were seen with HA-4-ATP-AuNFs-DOX, HA-4-ATP-AuNFs plus laser, or HA-4-ATP-AuNFs-DOX plus laser, particularly the combination of HA-4-ATP-AuNFs-DOX with laser, which led to almost all cells stained red. PI typically stains late apoptotic and necrotic cells as a result of dissociation of cell membranes[47] and Au nanoparticle–enabled PTT can cause both apoptosis and necrosis depending on the quantity of internalized nanoparticles, their intracellular location, and the amount of energy absorbed.[48] In this study, the 1064 nm laser-enabled photothermal effect of AuNFs may first cause more apoptotic damage to cancer cells and then progressed to necrosis with a power intensity of 1 W cm^{-2}.[49] The consistent results from MTT and live/dead staining suggest that the combination of NIR-II-induced heat and subsequent drug release from HA-4-ATP-AuNFs-DOX can significantly improve cancer therapeutic efficacy.

2.4. In Vivo PAT/SERS-Based Raman Imaging and Biodistribution of HA-4-ATP-AuNFs Nanosystems

Taking advantage of the recognized photostability and cytocompatibility of HA-4-ATP-AuNFs, we explored their utility for in vivo imaging. Based on the cellular study results (Figure 3e), it is reasonable to anticipate that HA-functionalized AuNFs could accumulate in tumors via active targeting and an enhanced permeability and retention (EPR) effect.[50] To assess the efficacy of HA-4-ATP-AuNFs for tumor imaging, a subcutaneous MDA-MB-231 breast cancer xenograft model was particularly chosen for its high mortality rate. MDA-MB-231 tumor-bearing mice intravenously administrated HA-4-ATP-AuNFs (20 mg kg^{-1}) had PA signals recorded at different postinjection times (0, 3, 6, 12, and 24 h) with an NIR-II wavelength of 1200 nm for PAT imaging (Figure 5a). PA signals in tumor tissue increased with time and reached a maximum around 12 h postinjection, confirmed by quantification of the PA signal intensity (Figure 5b). The demonstrated PA-imaging capability asserts the potential of HA-4-ATP-AuNFs as a contrast agent for NIR-II PA image-guided tumor therapy.

Similarly, in vivo SERS-based Raman imaging enabled by HA-4-ATP-AuNFs was also evaluated with MDA-MB-231 tumor-bearing mice. 12 h after intravenous administration of HA-4-ATP-AuNFs, tumors were resected and fixed for Raman imaging. As shown by Raman imaging (Figure 5c), the excised tumor harbored a high quantity of HA-4-ATP-AuNFs. Notably, Raman spectrum from position II of the tumor showed two characteristic Raman bands at 1085 and 1585 cm^{-1}, thus distinguishing tumor from the background (position I) (Figure 5d), in good agreement with in vitro Raman imaging results. To verify that HA-4-ATP-AuNFs indeed were accumulated to the tumor, tissue specimens

corroborated that positive Raman signals were processed for hematoxylin and eosin (H&E) staining and TEM analysis. The identified characteristic attributes, such as a high nuclear-to-cytoplasmic ratio, cellular crowding, and a necrotic core,[51] proved the formation of MDA-MB-231 tumor nodules (Figure 5e). Detection of porous AuNFs in resected tissue by TEM confirmed the specific accumulation of HA-4-ATP-AuNFs in the tumor (Figure 5e). In addition, we also performed high-magnification immunofluorescence imaging of the resected tumors to assess the distribution of DOX delivered by HA-4-ATP-AuNFs. As shown in Figure 5f, notable DOX (red fluorescence) was observed in tumor tissue, more specifically inside the tumor cells, indicating successful penetration of HA-4-ATP-AuNFs out of neovasculature labeled by CD31 and release of their cargo of DOX. Once again, HA-4-ATP-AuNFs can serve as a SERS-based contrast agent for Raman image- guided tumor therapy.

In order to better quantify tumor uptake and biodistribution of HA-4-ATP-AuNFs in tumor-bearing mouse, Au content in tumor and major organs (heart, liver, spleen, lung, and kidney) was analyzed via inductively coupled plasma mass spectrometry (ICP-MS). As shown in Figure S18 (Supporting Information), HA-4-ATP-AuNFs could efficiently accumulate into tumors with the respective enrichment rate of 4.8%, 9.4%, 13.4%, and 10.2% at 3, 6, 12, and 24 h after intravenous injection. After 12 h injection, Au content in the tumors reached its maximum, in a good agreement with PA-imaging data, confirming the good stealthy effect of these nanostructures in circulation for tumor accumulation.

2.5. In Vivo Tumor Therapeutic Effect

With the demonstrated advantages of HA-4-ATP-AuNFs, i.e., high accumulation in tumor tissue, efficient photothermal conversion in NIR-II, high drug payload, on-demand (light- and Hyal-1 triggered) release of loaded drug, as well as enabled-imaging modalities, image-guided photo-chemotherapy of MDA-MB-231 tumors was performed particularly using the NIR-II biowindow. Tumor-bearing mice, randomly divided into five groups ($n = 5$), were treated with: 1) PBS, 2) HA-4-ATP-AuNFs, 3) HA-4-ATP-AuNFs-DOX, 4) HA-4-ATP-AuNFs + 1064 nm laser, and 5) HA-4-ATP-AuNFs-DOX + 1064 nm laser. Mice of groups 4 and 5 were only exposed to 1064 nm laser irradiation at the time of 12 h postinjection of nanoparticles based on the finding from PA imaging (Figure 5a). As measured, the temperature of tumor sites dramatically increased to 55.4 °C after 10 min NIR-II laser irradiation (1 W cm^{-2}) of mice with HA-4-ATP-AuNFs (Figure 6a), sufficient for tumor ablation. It is noteworthy that the power of 1 W cm^{-2} should be safe to use, as no significant temperature elevation (36.6 °C) was observed with controls (PBS only).

The tumor progression after various treatments was monitored by recording the images of tumors and measuring the volume change. As shown in Figure 6b,c, HA-4-ATP-AuNFs alone (without laser irradiation) exhibited negligible therapeutic effect on tumors with no statistical difference from controls (PBS only). Tumor growth was partially suppressed for those mice treated with HA-4-ATP-AuNFs with 1064 nm laser (PTT) or HA-4-ATP-AuNFs-DOX alone (no laser, chemotherapy), and PTT seemed more effective than chemotherapy with current treatment conditions. Although a high Hyal-1 level is expected in MDA-MB-231 tumors,[52] which can trigger the release of DOX from HA-4-ATP-AuNFs-DOX

(no laser), the release significantly relies on the availability and concentration of Hyal-1 adjacent to nanoparticles and treatment efficiency is also affected by local DOX concentration. In contrast, photothermal ablation is only regulated by light and AuNFs. As anticipated, the highest tumor ablation was observed with HA-4-ATP-AuNFs-DOX in conjunction with 1064 nm laser irradiation, in which tumors were almost completely eliminated by 16 days, confirming the combined efficacy of photothermal- and chemotherapy in tumor treatment (Figure 6d). To better understand cell-level intratumor changes, histologic analysis was performed on resected tumors, revealing extensive necrosis in tumors with HA-4-ATP-AuNFs-DOX plus laser treatment as opposed to those with other treatments (Figure 6d). It is necessary to mention that the body weight of all mice remained comparable among all the experimental groups and showed steady increase over a period of 16 days (Figure S19, Supporting Information). Besides body weight, no abnormal histologic changes in major organs (lung, liver, kidney, spleen, and heart) were identified among control and other experimental groups (Figure 6e), implying the good biocompatibility of HA-4-ATP-AuNFs and HA-4-ATP-AuNFs-DOX. As shown in Figure S20 (Supporting Information), negligible changes could be observed in liver and renal function markers, including aspartate alaninetransaminase (ALT), aminotransferase (AST), alkaline phosphatase (ALP), and blood urea nitrogen (BUN), further demonstrating the good biosafety of this nanosystem.

3. Conclusion

In summary, we have established an effective theranostic strategy based on a novel gold nanostructure, i.e., AuNFs with mesopores, enabling PA/Raman image-guided photothermalchemo combination cancer therapy in the NIR-II biowindow. The use of liposomes as templates for AuNF synthesis not only guides and defines the formation of mesopores but also provides a simple and green fabrication route for Au nanostructures. The synthesized AuNFs exhibit marked photothermal effects in the second NIR biowindow in terms of high absorbance, improved photothermal stability, and high photothermal-conversion efficiency. As a result of the presence of high-density hotspots in AuNFs, the Raman scattering of 4-ATP conjugated on the surface of AuNFs can be used for Raman imaging with a significantly amplified “fingerprint.” Functionalization of the surface of AuNFs with HA offers a binding motif specifically targeting CD44-overexpressed tumor cells (MDA-MB-231), along with gatekeeping of drug molecules (DOX) loaded into mesopores. Both in vitro (cell-based) and in vivo (tumor-bearing xenograft) evaluations have demonstrated the high efficacy of HA-4-ATP-AuNFs-DOX for PA–Raman dual image-guided photo-chemotherapy of solid tumors in NIR-II, achieving almost complete tumor eradication. Collectively, the current nanosystems have shown versatile utility potentials, and further evaluation of their biosafety and loading efficiency of different therapeutics is essential for future clinical translation.

4. Experimental Section

Materials:

DPPC, cholesterol, and 4-ATP were purchased from Fisher Scientific (Waltham, MA, USA). DOX was obtained from Cayman Chemicals (Ann Arbor, MI, USA). Tetrachloroauric acid trihydrate ($HAuCl_4 \cdot 3H_2O$), AA, HA, and calcein AM/PI staining kit were purchased from Sigma–Aldrich (St Louis, MO). All chemicals were used as received without further treatment.

Synthesis of Liposomes:

Liposomes were prepared using the thin-film hydration method with modification.[22] Briefly, lipids (DPPC and cholesterol at a molar ratio of 55:45) were dissolved in chloroform and then placed in a high vacuum to remove residual organic solvent. The lipid film was hydrated (1 mg mL^{-1}) with an aqueous AA solution (300×10^{-3} M) via sonication at room temperature. The unilamellar liposomes were separated by centrifugation at 13 000 rpm for 15 min at 15 °C. The supernatant liposomes containing reducing agents were used for synthesis of AuNFs.

Synthesis of AuNFs:

AuNFs were synthesized via a simple and green template method. Typically, 0.4 mL of $HAuCl_4 \cdot 3H_2O$ solution (8×10^{-3} M) was added dropwise into the above liposome solutions (1 mL) and gently stirred for 1 h. During the reaction, color of the solution rapidly changed from milk white into blue gray. The unreacted residue and liposome templates were removed by centrifugation at 10 000 rpm for 10 min and rinsing with deionized (DI) water for three times. Obtained AuNFs were stored at 4 °C for future use.

Synthesis of HA-4-ATP-AuNFs-DOX Nanosystem:

To improve the reaction efficiency, HA-4-ATP was first synthesized. Briefly, 1 mL of 4-ATP solution (dimethyl sulfoxide (DMSO):DI water = 5:3) containing 40 mg of 4-ATP was added into HA solution (1.67 mg mL^{-1}, 30 mL) and pH of the mixture was adjusted to 4.0. 50.1 mg of EDC was then added into the mixture and stirred for 3 h at room temperature. Afterward, 7.5 mg of sodium borohydride was added into the solution and stirred for 1 h at 4 °C. The final solution was extracted with ethyl acetate three times, followed by sequential vacuum drying to obtain yellow-whitish HA-4-ATP powder. To modify AuNFs, 10 mg of HA-4-ATP powder was added into 1 mg of AuNFs dispersed in 4 mL of DI water. After sonication for 20 min and stirring overnight, excessive HA-4-ATP was removed by centrifugation (10 000 rpm, 10 min) and washing with DI water. The obtained HA-4-ATP-AuNFs were highly water soluble and stored at 4 °C for further use.

For DOX loading, AuNFs (0.2 mg mL^{-1}) were mixed with DOX at different concentrations in phosphate buffer (20×10^{-3} M, pH 8.0). After stirring at room temperature for 24 h, excessive unbounded DOX was removed by centrifugation at 10 000 rpm for 10 min and rinsing with DI water for several times.

Characterization:

TEM images were obtained with an FEI Titan Themis 200 TEM at an acceleration voltage of 200 kV. SEM images were obtained a Zeiss Auriga FIB-SEM. UV–vis–NIR absorption spectra were performed with a Shimadzu UV-3600 spectrophotometer. Using Beer's law ($A/L = \alpha C$), the AuNFs' extinction coefficient was extracted from the slope of a plot of A/L versus concentration (C). The optical extinction per cell length (A/L) was determined from the optical extinction intensity at 1064 nm. The size, polydispersity index, and zeta potential of nanoparticles were determined by dynamic light scattering (Zetasizer 3000HS; Malvern Instruments, Worcestershire, UK). FTIR spectra were recorded in a range of 400–4000 cm^{-1} at a 0.5–4 cm^{-1} resolution with a Bruker Vertex 80v vacuum FTIR spectrometer. A 1064 nm multimode pump laser (Shanghai Connect Fiber Optics Co. Ltd.) was used as the irradiation source for NIR-II photothermal effect. For in vitro PAT, HA-4-ATP-AuNFs at different concentrations (0, 0.1, 0.2, 0.4, 0.8, and 1 mg mL^{-1}) were added into 200 μL tubes for PA signal detection using a PA instrument (VisualSonics Vevo 2100 LAZR systems) with an excitation wavelength of 1200 nm.

Photothermal Performance of HA-4-ATP-AuNFs in the NIR-II Biowindow:

HA-4-ATP-AuNFs dispersed in deionized water at different concentrations (0, 50, 100, 150, and 200 μg mL^{-1}) were exposed to 1064 nm laser irradiation with a power intensity of 1.0 W cm^{-2}. The temperature and thermal images at different time durations were measured and recorded by a two-channel data logger thermometer and an infrared camera (FLIR TM A325SC camera), respectively.

NIR/Hyal-Triggered DOX Release from HA-4-ATP-AuNFs-DOX:

Release of DOX from HA-4-ATP-AuNFs-DOX was investigated using a dialysis approach. Briefly, 1 mL of HA-4-ATP-AuNFs-DOX (1 mg mL^{-1}) was placed in a dialysis bag (MWCO = 14 kDa) and respectively irradiated with or without a 1064 nm PTT laser (1 W cm^{-2}) at 1 and 4 h. To evaluate the gatekeeping effect of HA, HA-4-ATP-AuNFs-DOX aqueous buffer solutions (1 mg mL^{-1}) with and without Hyal-1 (150 U mL^{-1}) were also similarly placed in a dialysis bag and stirred at 37 °C. At designated time points, DOX released into the solutions was measured using a fluorescence spectrophotometry to establish the release profiles.

To further confirm NIR-triggered release, intracellular release of DOX was also studied. MDA-MB-231 cells (5×10^5 cells per well) were incubated with HA-4-ATP-AuNFs-DOX (100 μg mL^{-1}) for 2 h, and then irradiated with a 1064 nm NIR laser (1 W cm^{-2}) for 5 min. After culture for 2 h, cells were rinsed with PBS, fixed with 4% paraformaldehyde, and then examined using a fluorescence microscope.

In Vitro Targeting Ability of HA-4-ATP-AuNFs-DOX:

MDA-MB-231 tumor cells and HUVECs were used as model cells to determine the tumor-targeting capability of HA-modified AuNFs. Respective cells (5×10^5 cells per well) were cultured in Dulbecco's modified Eagle's medium (DMEM) or RPMI-1640 media with 10% fetal bovine serum and 1% streptomycin/penicillin for 24 h. The cells were rinsed with PBS and incubated with HA-4-ATP-AuNFs-DOX (100 μg mL^{-1}) for 4 h. To verify the specificity

of HA binding to CD44, a separate study was also performed to incubate the cells with free HA (2 mg mL^{-1}) for 1 h prior to the incubation with HA-4-ATP-AuNFs-DOX. Upon further rinsing with PBS, the culture was fixed with paraformaldehyde solution (4%) and observed with a Nikon 80*i* epifluorescence microscope.

To identify intracellular distribution of AuNFs in tumor cells, MDA-MB-231 cells were seeded into 6-well plates (1×10^6 cells per well) and incubated with HA-4-ATP-AuNFs (100 μg mL^{-1}) for 4 h. Upon rinse with PBS to remove excessive nanoparticles, the cells were trypsinized, washed with PBS, and centrifuged to obtain cell pellets. The pellets were fixed with 2.5% glutaraldehyde for 24 h. Afterward, the pellets were postfixed with osmium tetroxide for 1 h and then rinsed with distilled water. After dehydration in a series of graded ethanol, the pellets were embedded in epoxy for 24 h, and then cut into thin sections (60 nm) for TEM examination.

In Vitro Antitumor Performance:

MDA-MB-231 cells were seeded into a 96-well plate at a density of 1×10^4 cells per well and cultured for 24 h at 37 °C. Media was replaced with fresh media containing free DOX or HA-4-ATP-AuNFs-DOX at different DOX concentrations. After 18 h incubation, the cells were irradiated with or without a 1064 nm NIR laser (1 W cm^{-2}) for 5 min and further incubated for another 6 h. Upon replacement with fresh media containing MTT (0.5 mg mL^{-1}), the cells were further cultured for 4 h. Then, 200 μL of DMSO was added to each well to extract the formazan and absorbance at 490 nm was measured using a microplate reader.

CI value was used to evaluate the synergistic effect of two drugs and calculated using the following equation: $CI = IC_{50}(A)_{pair}/IC_{50}(A) + IC_{50}(B)_{pair}/IC_{50}(B)$, where IC_{50} is 50% inhibition concentration for each individual drug (A or B) or for the drug given as an A–B pair. $CI < 1$, $CI = 1$, and $CI > 1$ indicates synergistic, additive, and antagonistic, respectively.

A calcein-AM/PI assay was also performed to study the in vitro antitumor activity of HA-4-ATP-AuNFs-DOX. Briefly, MDA-MB-231 cells seeded in 6-well plates were similarly treated with HA-4-ATP-AuNFs-DOX and 1064 nm laser irradiation (1 W cm^{-2}, 5 min) as described above. Resulting cells were stained with calcein-AM/PI and examined under the fluorescence microscope.

In Vitro SERS-Based Cell Raman Imaging:

To delineate cells with SERS-based Raman imaging, MDA-MB-231 cells (2×10^5) seeded on 2 cm × 2 cm coverslips for 24 h were incubated with HA-4-ATP-AuNFs (100 μg mL^{-1}) for 4 h. The cells were then extensively rinsed with PBS and fixed with 4% paraformaldehyde for 20 min. Upon further rinsing with PBS, samples were observed under a Raman system (WITec Confocal Raman Microscope alpha300R). Raman images of cells were performed in StreamLine high-speed acquisition mode (50 mW, 100× objective) with 1 μm step size and 1 s exposure time. Characteristic peak of HA-4-ATP-AuNFs at 1585 cm^{-1} was selected for image processing.

Tumor Model:

6–8 weeks old female Balb/c nude mice (≈20 g) purchased from the Department of Experimental Animals (Xiamen University) were used to generate the MDA-MB-231 xenograft tumor models. Briefly, MDA-MB-231 cells (2×10^6) suspended in 100 μL of PBS were subcutaneously injected to the back of each mouse. When the tumor volume reached ≈60 mm^3, the mice were used for in vivo experiments. All the animal experiments were carried out in accordance with the guidelines evaluated and approved by the ethics committee of Xiamen University.

In Vivo NIR-II PAT and SERS-Based Raman Imaging and Biodistribution:

For PAT, HA-4-ATP-AuNFs at a concentration of 1 mg mL^{-1} were intravenously injected into MDA-MB-231 tumor-bearing mice. The tumor region was imaged at different time points via a visual sonic system (VisualSonics Vevo 2100 LAZR systems) with an excitation wavelength at 1200 nm.

For SERS-based Raman imaging, MDA-MB-231 tumor-bearing mice were intravenously injected with HA-4-ATP-AuNFs (100 μL, 1 mg mL^{-1}). After 12 h circulation, the tumors were collected for Raman imaging. Raman imaging was performed with an inVia Raman microscope (Renishaw) equipped with a 785 nm diode laser. Raman scanning was performed in StreamLine high-speed acquisition mode (100 mW, 5× objective) with 70 μm step size and 1 s exposure time. The characteristic band of HA-4-ATP-AuNFs at 1585 cm^{-1} was selected for image processing.

The biodistribution of HA-4-ATP-AuNFs in tumor and major organs (heart, liver, spleen, lung, and kidney) was evaluated in the tumor-bearing mice ($n = 3$). HA-4-ATP-AuNFs at the dose of 20 mg kg^{-1} were intravenously injected into the MDA-MB-231 tumor-bearing mice. Then, at different time intervals (3, 6, 12, and 24 h) mice were sacrificed, and the dissected tissues were weighed, homogenized, and treated with aqua regia. Quantitative analysis of Au element was carried out by ICP-OES. The biodistribution of HA-4-ATP-AuNFs in different tissues was calculated as the percentage of injected dose per gram of tissue (%ID g^{-1}).

In Vivo Combination Therapy:

To determine the combined NIR-II PTT and chemotherapeutic effect of HA-4-ATP-AuNFs in vivo, MDA-MB-231 tumor-bearing mice were stochastically divided into five groups ($n = 5$): 1) PBS, 2) HA-4-ATP-AuNFs (1 mg mL^{-1}, 100 μL), 3) HA-4-ATPAuNFs-DOX (1 mg mL^{-1}, 100 μL), 4) HA-4-ATP-AuNFs (1 mg mL^{-1}, 100 μL) + laser, and 5) HA-4-ATP-AuNFs-DOX (1 mg mL^{-1}, 100 μL) + laser. After 12 h, tail intravenous injection of nanoparticles, the tumor region of the mice was irradiated with 1064 nm laser (1 W cm^{-2}) for 10 min. The mice in the groups intravenously injected with PBS and HA-4-ATP-AuNFs were used for infrared thermal imaging. The tumor volume and body weight of mice were recorded every 2 days for 16 days. The tumor volume was calculated using the following equation: tumor volume = length × $width^2/2$. At the end of the experiments, sacrificed mice were dissected, and the tumors and major organs were collected for histological analysis. For biochemical analyses of liver and kidney functions, the blood of mice was collected and

serum was obtained. The levels of the following enzymes, including ALT, ALP, AST, and BUN, in the serum were determined by enzyme-linked immunosorbent assay.

Statistical Analysis:

All quantitative results were obtained from at least three samples. Data were expressed as the mean ± standard deviation (SD). GraphPad Prism software (version 6.0, GraphPad Software, Inc., La Jolla, CA, USA) was used for statistical analysis. Comparisons of two groups were made with an unpaired Student's *t*-test. Multiple comparisons were performed using one-way analysis of variance (ANOVA) and Tukey's post-hoc analysis. The minimum significance level was set at $*p < 0.05$, $**p < 0.01$.

Supplementary Material

Refer to Web version on PubMed Central for supplementary material.

Acknowledgements

This study was financially supported by National Science Foundation (NSF-DMR award number 1508511), NIAMS (award number 1R01AR067859), and National Science Foundation of China (Grant Nos. U190420008 and 31870994). The authors would also like to thank Dr. Tong Wang and Sheng Zhang from the Advanced Science Research Center at Graduate Center of CUNY for analyzing the TEM images. The authors are also grateful to the help from Thomas Cattabiani (Stevens Institute of Technology) for proofreading.

References

[1]. Vankayala R, Hwang KC, Adv. Mater 2018, 30, 1706320.

[2]. a)Christopher P, Xin H, Linic S, Nat. Chem 2011, 3, 467; [PubMed: 21602862] b)Cheng L, Wang C, Feng L, Yang K, Liu Z, Chem. Rev 2014, 114, 10869; [PubMed: 25260098] c)Tang W, Dong Z, Zhang R, Yi X, Yang K, Jin M, Yuan C, Xiao Z, Liu Z, Cheng L, ACS Nano 2019, 13, 284. [PubMed: 30543399]

[3]. Dreaden EC, Alkilany AM, Huang X, Murphy CJ, El-Sayed MA, Chem. Soc. Rev 2012, 41, 2740. [PubMed: 22109657]

[4]. Guo L, Wu X, Liu L, Kuang H, Xu C, Small 2018, 14, 1701782.

[5]. Wu Y, Ali MRK, Chen K, Fang N, El-Sayed MA, Nano Today 2019, 24, 120.

[6]. Vigderman L, Zubarev ER, Adv. Drug Delivery Rev 2013, 65, 663.

[7]. Aioub M, El-Sayed MA, J. Am. Chem. Soc 2016, 138, 1258. [PubMed: 26746480]

[8]. a)Xiang H, Lin H, Yu L, Chen Y, ACS Nano 2019, 13, 2223; [PubMed: 30624041] b)Antaris AL, Chen H, Cheng K, Sun Y, Hong G, Qu C, Diao S, Deng Z, Hu X, Zhang B, Zhang X, Yaghi OK, Alamparambil ZR, Hong X, Cheng Z, Dai H, Nat. Mater 2016, 15, 235; [PubMed: 26595119] c)Han X, Huang J, Jing X, Yang D, Lin H, Wang Z, Li P, Chen Y, ACS Nano 2018, 12, 4545; [PubMed: 29697960] d)Yang K, Feng L, Shi X, Liu Z, Chem. Soc. Rev 2013, 42, 530; [PubMed: 23059655] e)Cao Y, Wu T, Zhang K, Meng X, Dai W, Wang D, Dong H, Zhang X, ACS Nano 2019, 13, 1499. [PubMed: 30677286]

[9]. Ji M, Xu M, Zhang W, Yang Z, Huang L, Liu J, Zhang Y, Gu L, Yu Y, Hao W, An P, Zheng L, Zhu H, Zhang J, Adv. Mater 2016, 28, 3094. [PubMed: 26913692]

[10]. Maestro LM, Haro-Gonzalez P, del Rosal B, Ramiro J, Caamano AJ, Carrasco E, Juarranz A, Sanz-Rodriguez F, Sole JG, Jaque D, Nanoscale 2013, 5, 7882. [PubMed: 23852326]

[11]. Lin H, Gao S, Dai C, Chen Y, Shi J, J. Am. Chem. Soc 2017, 139, 16235. [PubMed: 29063760]

[12]. Wang X, Ma Y, Sheng X, Wang Y, Xu H, Nano Lett 2018, 18, 2217. [PubMed: 29528661]

[13]. a)Schlucker S, Angew. Chem., Int. Ed 2014, 53, 4756;b)Pal S, Ray A, Andreou C, Zhou Y, Rakshit T, Wlodarczyk M, Maeda M, Toledo-Crow R, Berisha N, Yang J, Hsu HT, Oseledchyk A, Mondal J, Zou S, Kircher MF, Nat. Commun 2019, 10, 1926. [PubMed: 31028250]

[14]. a)Andreou C, Neuschmelting V, Tschaharganeh DF, Huang CH, Oseledchyk A, Iacono P, Karabeber H, Colen RR, Mannelli L, Lowe SW, Kircher MF, ACS Nano 2016, 10, 5015; [PubMed: 27078225] b)Qiu Y, Zhang Y, Li M, Chen G, Fan C, Cui K, Wan JB, Han A, Ye J, Xiao Z, ACS Nano 2018, 12, 7974. [PubMed: 30080395]

[15]. a)Yang S, Dai X, Stogin BB, Wong TS, Proc. Natl. Acad. Sci. USA 2016, 113, 268; [PubMed: 26719413] b)Dinish US, Song Z, Ho CJH, Balasundaram G, Attia ABE, Lu X, Tang BZ, Liu B, Olivo M, Adv. Funct. Mater 2015, 25, 2316;c)Qu L, Wang N, Xu H, Wang W, Liu Y, Kuo L, Yadav TP, Wu J, Joyner J, Song Y, Li H, Lou J, Vajtai R, Ajayan PM, Adv. Funct. Mater 2017, 27, 1701714.

[16]. Lin Q, Yang Y, Ma Y, Zhang R, Wang J, Chen X, Shao Z, Nano Lett 2018, 18, 7485. [PubMed: 30444622]

[17]. von Maltzahn G, Centrone A, Park JH, Ramanathan R, Sailor MJ, Hatton TA, Bhatia SN, Adv. Mater 2009, 21, 3175. [PubMed: 20174478]

[18]. Ge X, Song ZM, Sun L, Yang YF, Shi L, Si R, Ren W, Qiu X, Wang H, Biomaterials 2016, 108, 35. [PubMed: 27619238]

[19]. Cheheltani R, Ezzibdeh RM, Chhour P, Pulaparthi K, Kim J, Jurcova M, Hsu JC, Blundell C, Litt HI, Ferrari VA, Allcock HR, Sehgal CM, Cormode DP, Biomaterials 2016, 102, 87. [PubMed: 27322961]

[20]. Miao T, Ju X, Zhu Q, Wang Y, Guo Q, Sun T, Lu C, Han L, Adv. Funct. Mater 2019, 29, 1900259.

[21]. Liu Y, Zhi X, Yang M, Zhang J, Lin L, Zhao X, Hou W, Zhang C, Zhang Q, Pan F, Alfranca G, Yang Y, de la Fuente JM, Ni J, Cui D, Theranostics 2017, 7, 1650. [PubMed: 28529642]

[22]. Chen KJ, Chaung EY, Wey SP, Lin KJ, Cheng F, Lin CC, Liu HL, Tseng HW, Liu CP, Wei MC, Liu CM, Sung HW, ACS Nano 2014, 8, 5105. [PubMed: 24742221]

[23]. Chang M, Lu S, Zhang F, Zuo T, Guan Y, Wei T, Shao W, Lin G, Colloids Surf., B 2015, 129, 175.

[24]. Sohn K, Kim F, Pradel KC, Wu J, Peng Y, Zhou F, Huang J, ACS Nano 2009, 3, 2191. [PubMed: 19621938]

[25]. Mandal S, Arumugam SK, Adyanthaya SD, Pasricha R, Sastry M, J. Mater. Chem 2004, 14, 43.

[26]. Aslam M, Fu L, Su M, Vijayamohanan K, Dravid VP, J. Mater. Chem 2004, 14, 1795.

[27]. a)Zheng T, Li GG, Zhou F, Wu R, Zhu JJ, Wang H, Adv. Mater 2016, 28, 8218; [PubMed: 27459898] b)Liu K, Bai Y, Zhang L, Yang Z, Fan Q, Zheng H, Yin Y, Gao C, Nano Lett 2016, 16, 3675. [PubMed: 27192436]

[28]. Zhou J, Jiang Y, Hou S, Upputuri PK, Wu D, Li J, Wang P, Zhen X, Pramanik M, Pu K, Duan H, ACS Nano 2018, 12, 2643. [PubMed: 29438610]

[29]. Zhu X, Feng W, Chang J, Tan YW, Li J, Chen M, Sun Y, Li F, Nat. Commun 2016, 7, 10437. [PubMed: 26842674]

[30]. Xie H, Li Z, Sun Z, Shao J, Yu XF, Guo Z, Wang J, Xiao Q, Wang H, Wang QQ, Zhang H, Chu PK, Small 2016, 12, 4136. [PubMed: 27329254]

[31]. Ding SY, You EM, Tian ZQ, Moskovits M, Chem. Soc. Rev 2017, 46, 4042. [PubMed: 28660954]

[32]. Rodríguez-Lorenzo L, Álvarez-Puebla RA, Pastoriza-Santos I, Mazzucco S, Stephan O, Kociak M, Liz-Marzán LM, García de Abajo FJ, J. Am. Chem. Soc 2009, 131, 4616. [PubMed: 19292448]

[33]. Alexander KD, Skinner K, Zhang S, Wei H, Lopez R, Nano Lett 2010, 10, 4488. [PubMed: 20923232]

[34]. Yang M, Alvarez-Puebla R, Kim HS, Aldeanueva-Potel P, Liz-Marzan LM, Kotov NA, Nano Lett 2010, 10, 4013. [PubMed: 20738117]

[35]. Xue Y, Li X, Li H, Zhang W, Nat. Commun 2014, 5, 4348. [PubMed: 25000336]

[36]. Yan Y, Zuo X, Wei D, Stem Cells Transl. Med 2015, 4, 1033. [PubMed: 26136504]

[37]. Kemp MM, Kumar A, Mousa S, Park T, Ajayan P, Kubotera N, Mousa SA, Linhardt RJ, Biomacromolecules 2009, 10, 589. [PubMed: 19226107]

[38]. Xu W, Qian J, Hou G, Suo A, Wang Y, Wang J, Sun T, Yang M, Wan X, Yao Y, ACS Appl. Mater. Interfaces 2017, 9, 36533. [PubMed: 28975790]

[39]. Chen Q, Liu G, Liu S, Su H, Wang Y, Li J, Luo C, Trends Pharmacol. Sci 2018, 39, 59. [PubMed: 29153879]

[40]. Lin LS, Yang X, Zhou Z, Yang Z, Jacobson O, Liu Y, Yang A, Niu G, Song J, Yang HH, Chen X, Adv. Mater 2017, 29, 1606681.

[41]. Liu T, Wang C, Gu X, Gong H, Cheng L, Shi X, Feng L, Sun B, Liu Z, Adv. Mater 2014, 26, 3433. [PubMed: 24677423]

[42]. Wang Y, Sun Y, Wang J, Yang Y, Li Y, Yuan Y, Liu C, ACS Appl. Mater. Interfaces 2016, 8, 17166. [PubMed: 27314423]

[43]. Sheridan C, Kishimoto H, Fuchs RK, Mehrotra S, Bhat-Nakshatri P, Turner CH, Goulet R Jr., Badve S, Nakshatri H, Breast Cancer Res 2006, 8, R59. [PubMed: 17062128]

[44]. Chen C, Zhao S, Karnad A, Freeman JW, J. Hematol. Oncol 2018, 11, 64. [PubMed: 29747682]

[45]. Yang D, Pang X, He Y, Wang Y, Chen G, Wang W, Lin Z, Angew. Chem., Int. Ed 2015, 54, 12091.

[46]. Zhang L, Li S, Chen X, Wang T, Li L, Su Z, Wang C, Adv. Funct. Mater 2018, 28, 1803815.

[47]. Kroemer G, Dallaporta B, Resche-Rigon M, Annu. Rev. Physiol 1998, 60, 619. [PubMed: 9558479]

[48]. Perez-Hernandez M, del Pino P, Mitchell SG, Moros M, Stepien G, Pelaz B, Parak WJ, Galvez EM, Pardo J, de la Fuente JM, ACS Nano 2015, 9, 52. [PubMed: 25493329]

[49]. Tortiglione C, Iachetta R, Ann. Transl. Med 2016, 4, S51. [PubMed: 27868019]

[50]. Hobbs SK, Monsky WL, Yuan F, Roberts WG, Griffith L, Torchilin VP, Jain RK, Proc. Natl. Acad. Sci. USA 1998, 95, 4607. [PubMed: 9539785]

[51]. Du J, Wang XF, Zhou QM, Zhang TL, Lu YY, Zhang H, Su SB, Oncol. Rep 2013, 30, 685. [PubMed: 23708383]

[52]. Tan JX, Wang XY, Li HY, Su XL, Wang L, Ran L, Zheng K, Ren GS, Int. J. Cancer 2011, 128, 1303. [PubMed: 20473947]

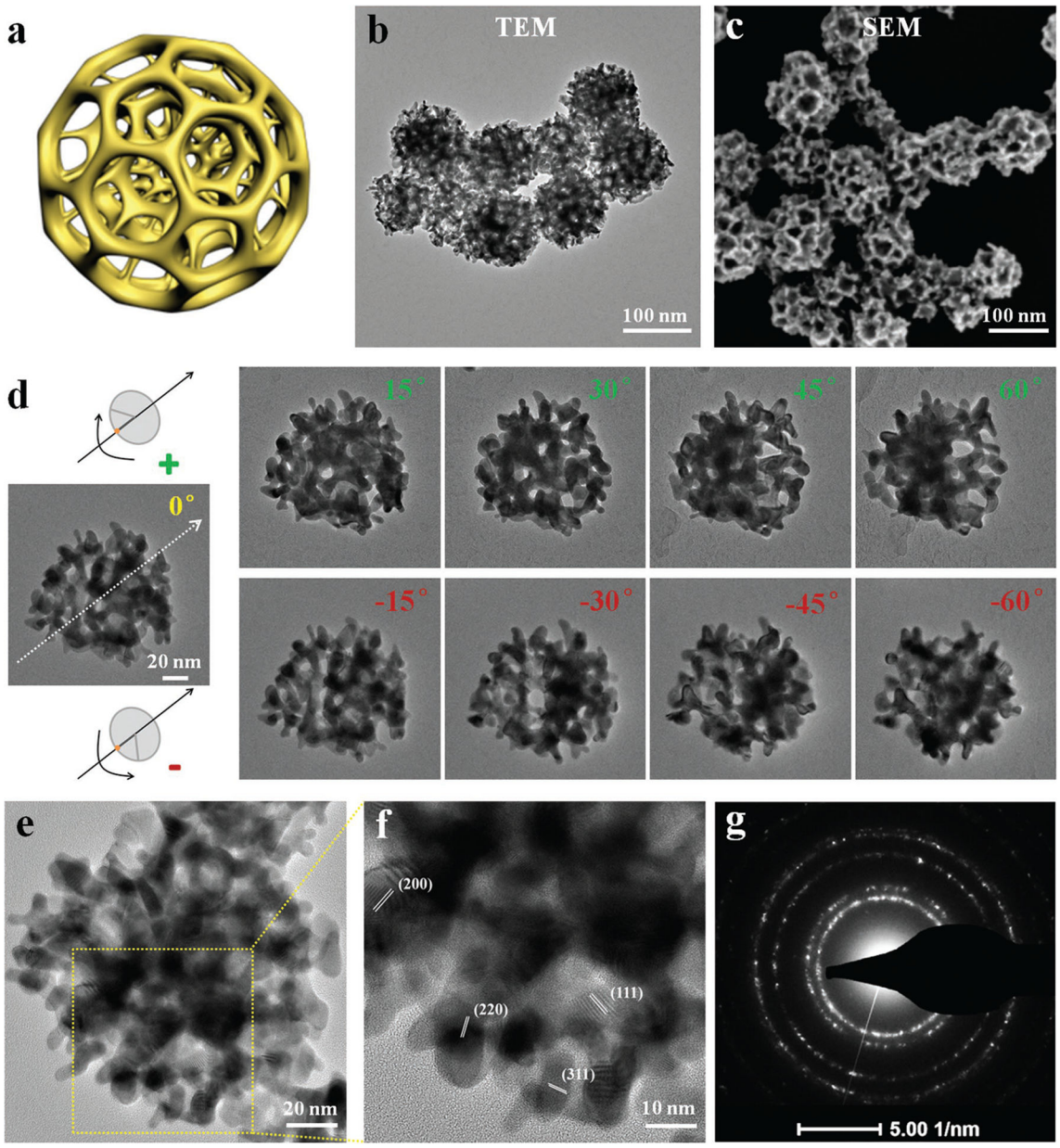

Figure 1.

a) Schematic illustration of porous AuNFs. b) TEM image of AuNFs. c) SEM image of porous AuNFs. d) A series of TEM micrographs of individual AuNFs tilted at different angles (−60°, −45°, −30°, −15°, 0°, 15°, 30°, 45°, and 60°, respectively). e,f) HRTEM images of AuNFs to show crystallinity. g) Electron diffraction patterns recorded from one AuNF.

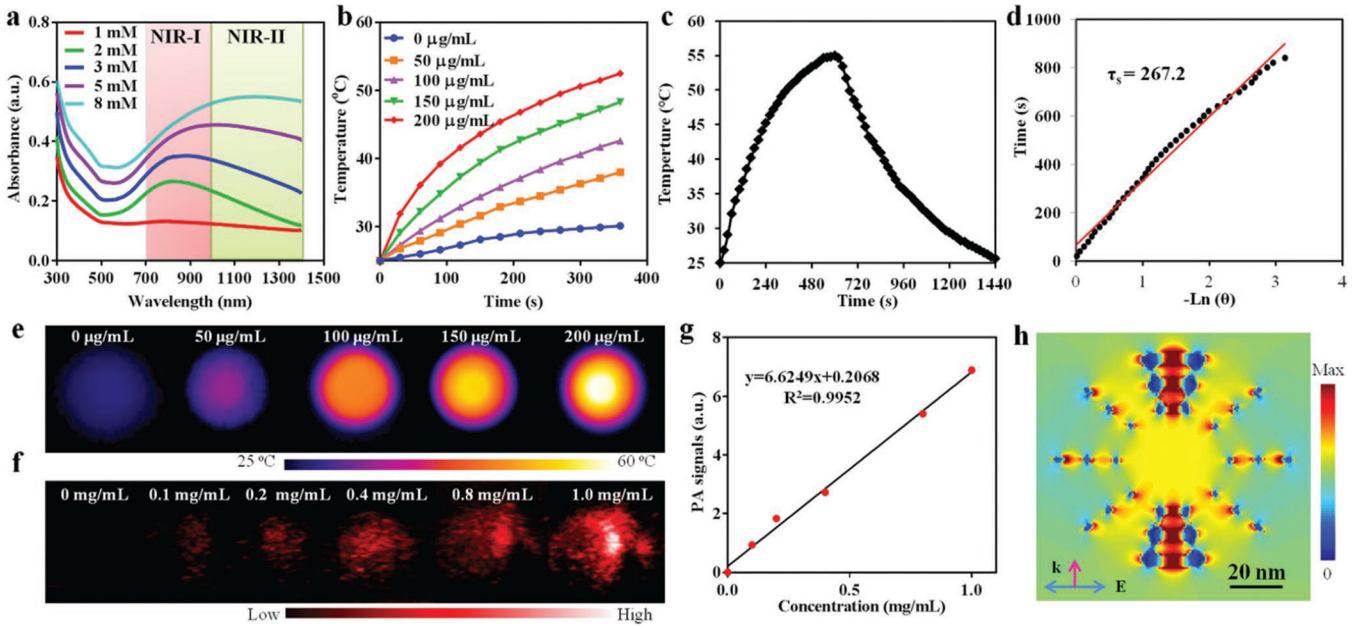

Figure 2.

a) UV–vis–NIR spectra of AuNFs with the increasing of gold precursor ($HAuCl_4$) concentration, showing a bathochromic shift of localized surface plasmon resonance (LSPR) peaks. b) Concentration-dependent of photothermal effect of AuNFs under 1064 nm laser irradiation (1 W cm^{-2}). c) Time-resolved photothermal effect of aqueous AuNFs (200 μg mL^{-1}) with 1064 nm laser irradiation (1 W cm^{-2}) for 600 s, and then cut off with stable temperature. d) Plot of cooling time versus negative natural logarithm of the temperature driving force obtained from the cooling stage. e) Photothermal images of AuNFs at different concentrations under 1064 nm laser irradiation (1 W cm^{-2}, 360 s). f) Photoacoustic images of AuNFs at different concentrations. g) Linear correlation between photoacoustic intensity and concentration of AuNF aqueous solutions. h) Simulated near-field electromagnetic field distribution of AuNFs irradiated with a scattered-field plane wave. All simulations were performed with Lumerical FDTD Solutions.

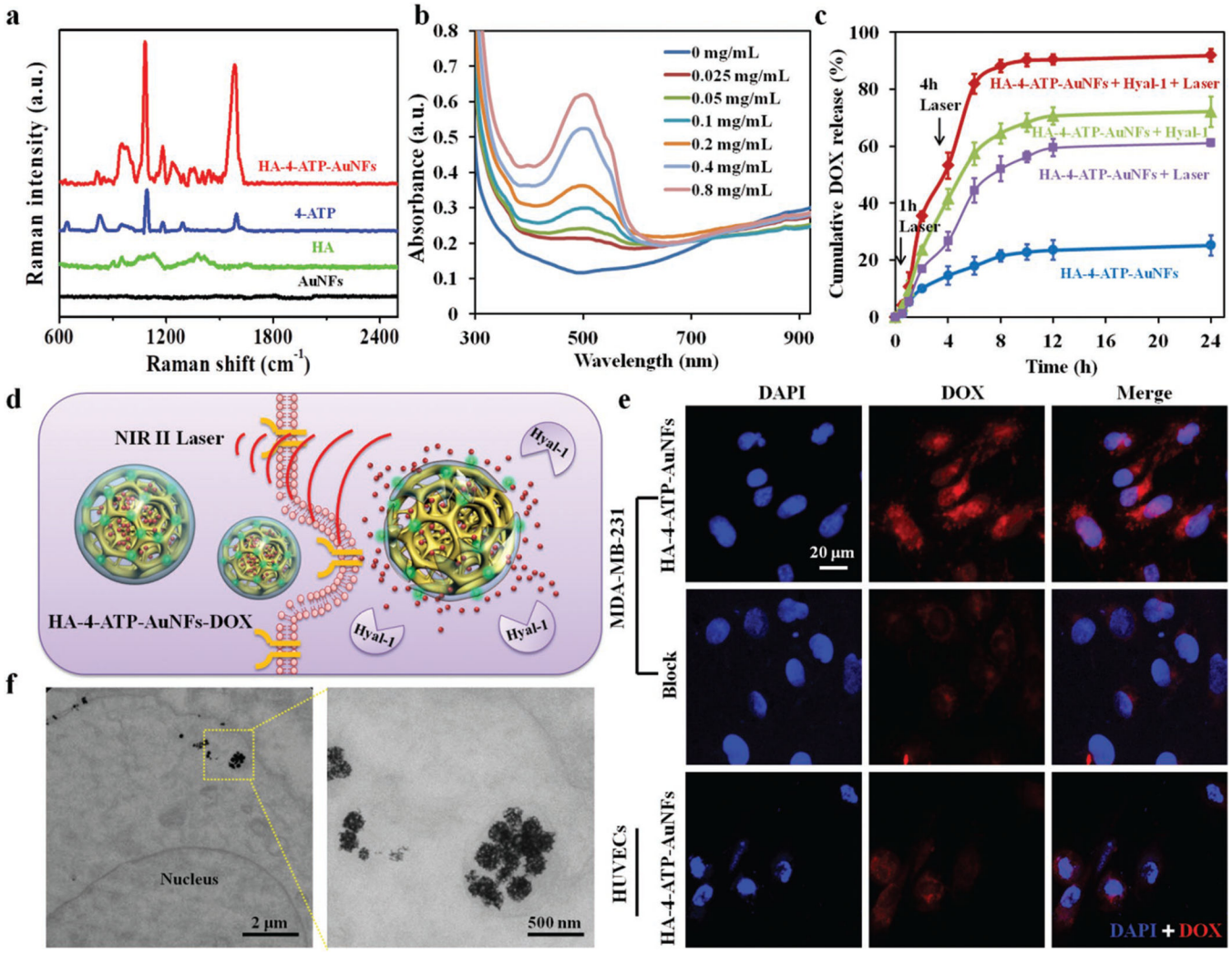

Figure 3.

a) Raman spectra of different samples. b) UV–vis–NIR spectra of DOX-loaded HA-4-ATP-AuNFs obtained at different drug-loading concentrations after removal of excessive free drug molecules. c) Release profiles of DOX from HA-4-ATP-AuNFs with or without Hyaluronidases 1 (Hyal-1)) at 37 °C or under 1064 nm laser irradiation (1 W cm^{-2}) at the time points of 1 and 4 h, respectively. d) Schematic illustration of the HA-targeting-directed photothermal cell ablation and drug release in the NIR-II biowindow. e) Cell uptake of DOX-loaded HA-4-ATP-AuNFs by MDA-MB-231 cells and HUVECs. HA-4-ATP-AuNF-DOX is effectively internalized by MDA-MB-231 cells via a CD44-mediated pathway. Due to the lack of CD44 expression, few AuNFs were internalized into HUVECs. CD44-mediated cell internalization of HA-4-ATP-AuNFs-DOX can be effectively inhibited by excessive free HA. f) TEM images showing intracellular localization of HA-4-ATP-AuNFs in MDA-MB-231 cells after a 4 h incubation.

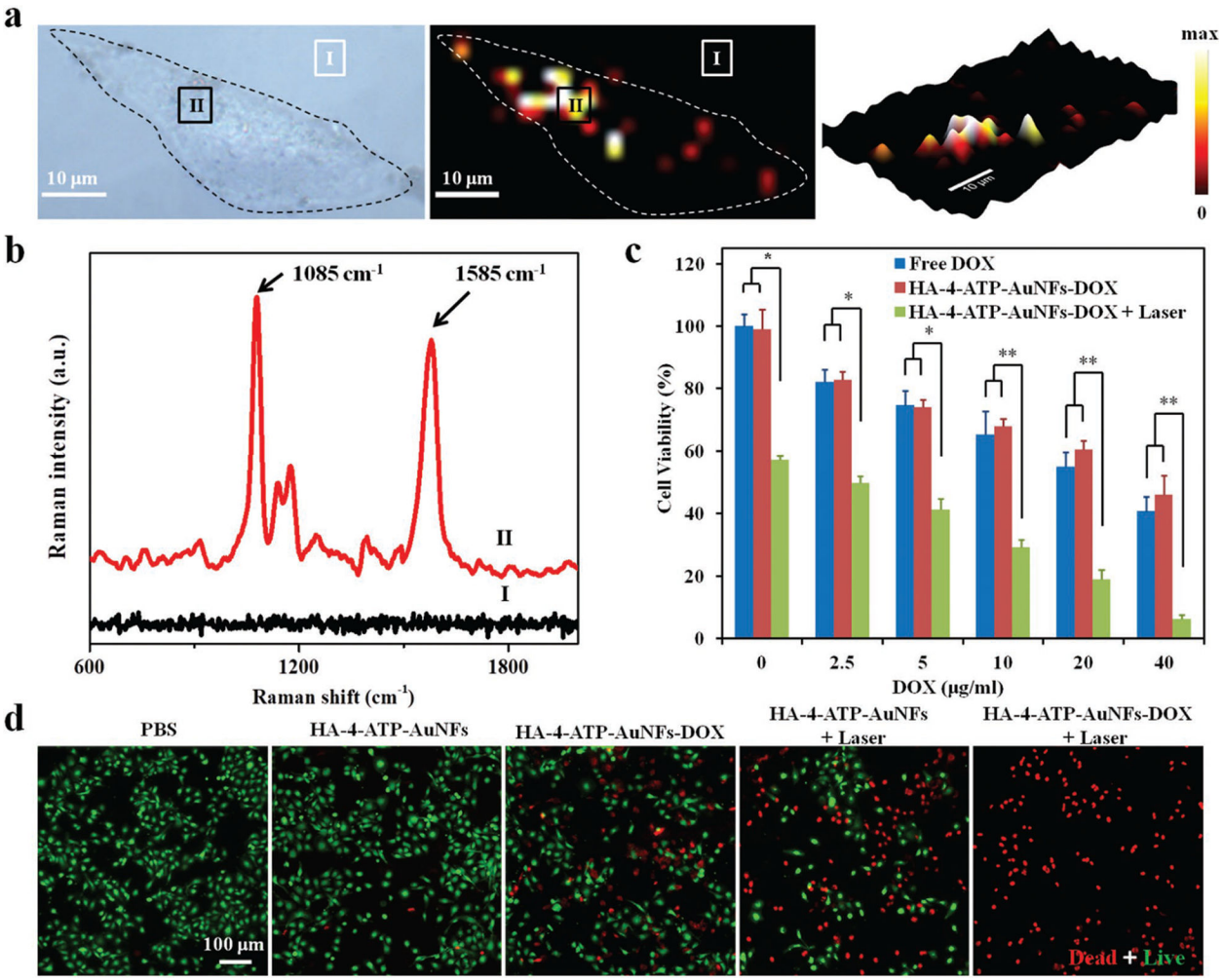

Figure 4.

a) Raman imaging of MDA-MB-231 cells incubated with HA-4-ATP-AuNFs. b) Raman spectra of HA-4-ATP-AuNFs at points I and II. c) Cell viabilities of MDA-MB-231 cells with different treatments. *$p < 0.05$, **$p < 0.01$. d) Fluorescent microscopy images of live/dead MDA-MB-231 cells treated with different conditions with or without NIR laser irradiation (1064 nm, 1 W cm^{-2}). Live cells were stained green with calcein-AM and dead cells were stained red with PI.

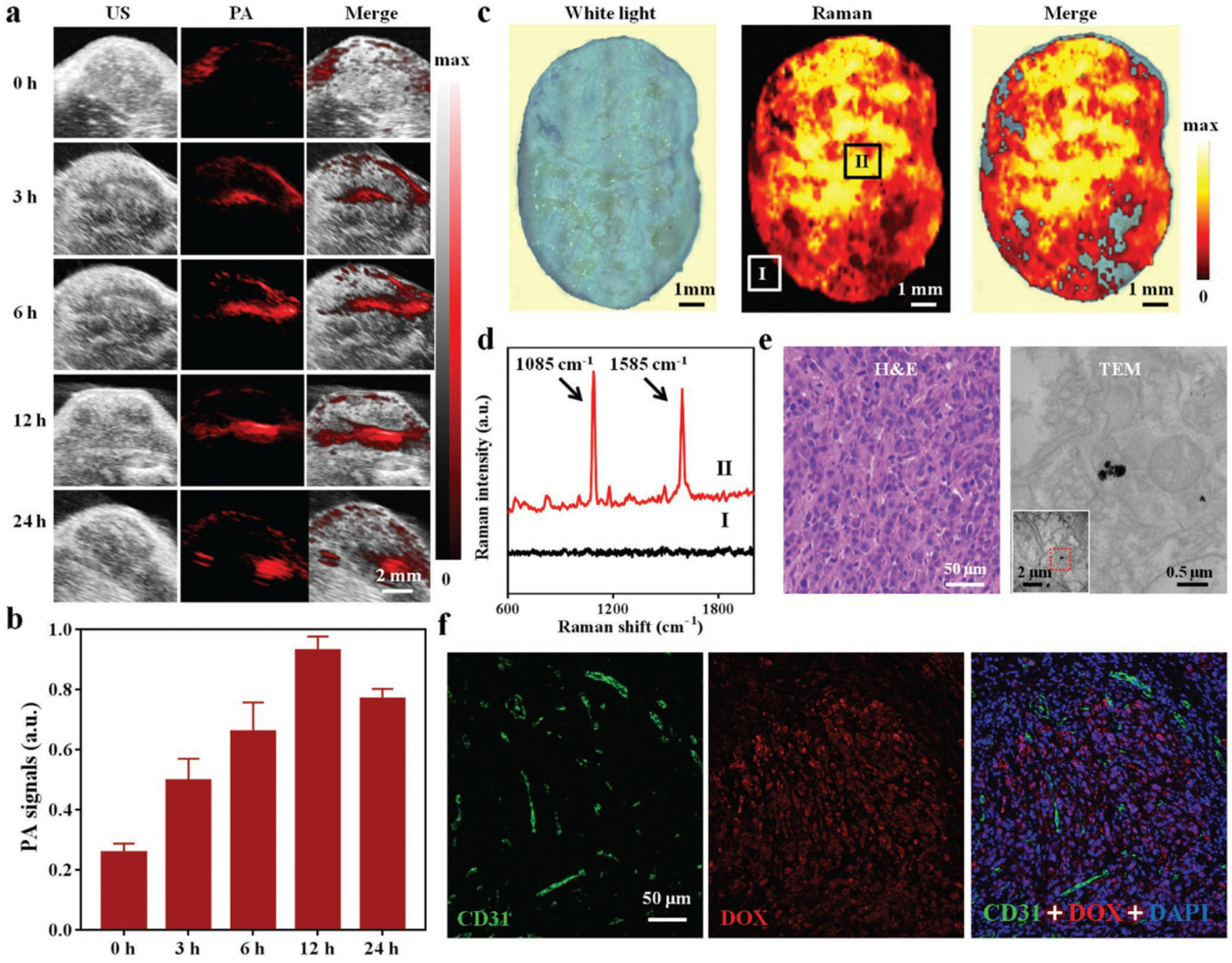

Figure 5.

a) PA images of HA-4-ATP-AuNFs at the tumor site at varied time points postinjection (0, 3, 6, 12, and 24 h). b) Average PA intensity at the tumor site in panel (a). c) Raman imaging of excised tumor tissue. Colors represent intensity in the characteristic Raman band of HA-4-ATP-AuNFs at 1585 cm^{-1}. d) Raman spectra acquired from positions I and II. e) Hematoxylin and eosin (H&E) staining and TEM images of tissue acquired from position II. TEM examination confirmed the presence of HA-4-ATP-AuNFs in tumor tissue. f) Immunofluorescence images of resected MDA-MB-231 tumor for DOX localization (red channel). Frozen sections were stained with CD31 antibody (green channel) for neovasculature.

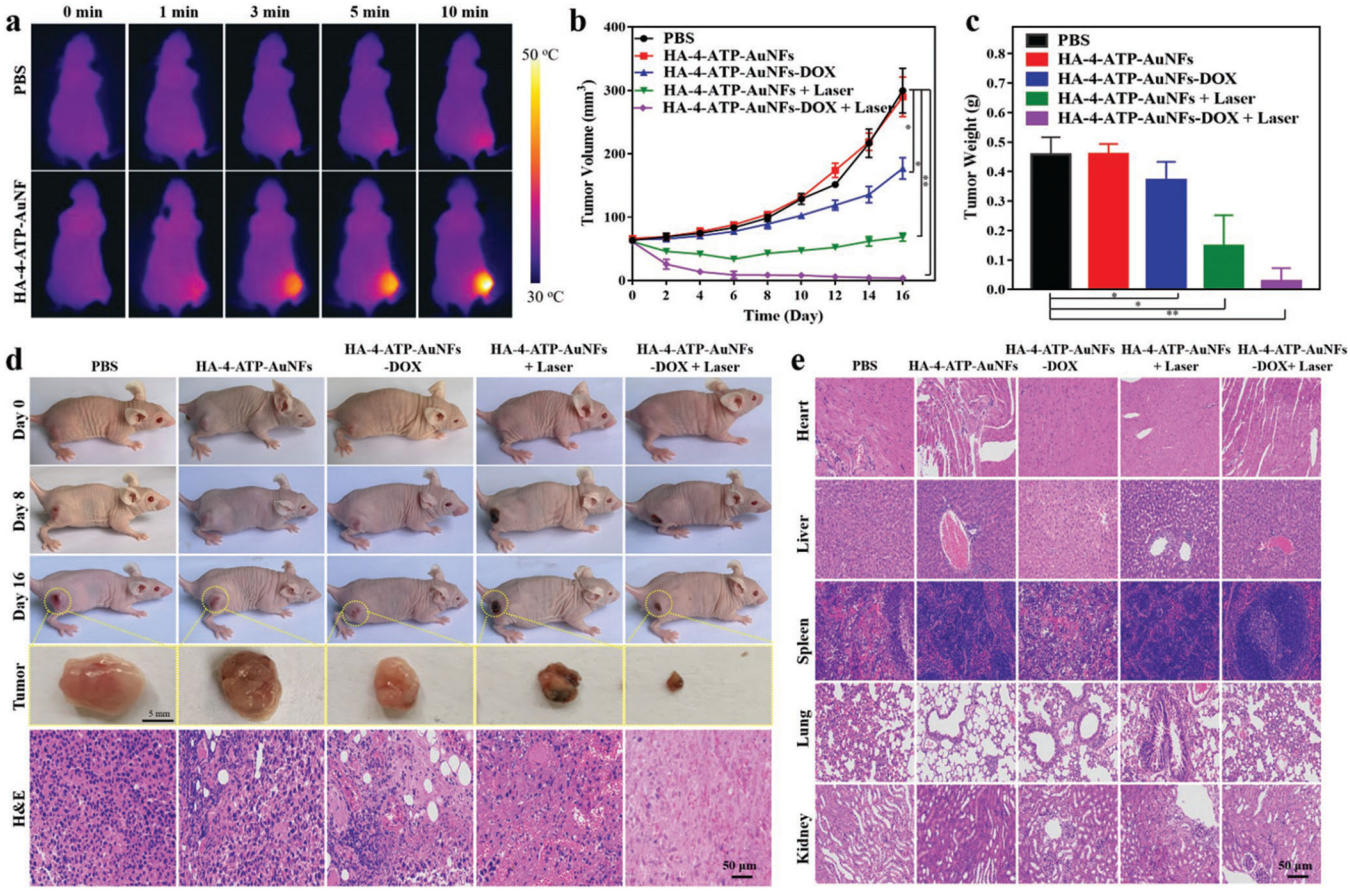

Figure 6.

a) Photothermal images of MDA-MB-231 tumor-bearing mice exposed to NIR-II laser (1064 nm, 1 W cm^{-2}, 10 min) after intravenous injection with PBS and HA-4-ATP-AuNFs, respectively. b) Time-resolved tumor growth (volume-based) in mice with different treatments. c) Final tumor weight resected from mice with different treatments. *$p < 0.05$ and **$p < 0.01$. d) Digital images and H&E-stained cross sections of resected tumors from different groups treated with PBS, HA-4-ATP-AuNFs only, HA-4-ATP-AuNFs-DOX, HA-4-ATP-AuNFs plus NIR-II laser, and HA-4-ATP-AuNFs-DOX plus NIR-II laser in different time intervals. e) H&E staining of major organs from different groups.

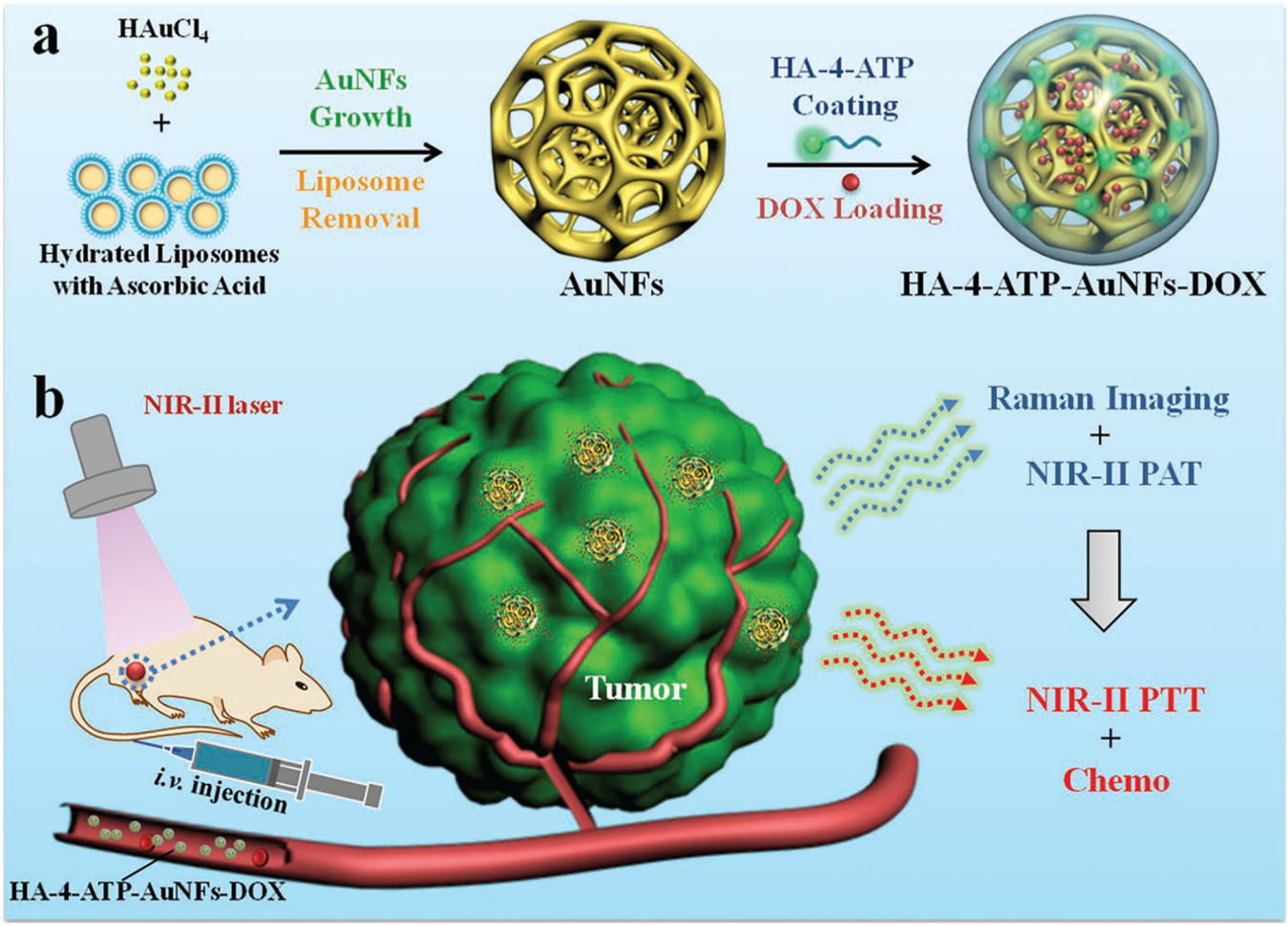

Scheme 1.

a) Fabrication of HA-4-ATP-AuNFs-DOX nanosystem. b) Schematic illustration of HA-4-ATP-AuNFs-DOX for SERS-based Raman–photoacoustic imaging and combined photo-chemo-tumor therapy in the second near-infrared biowindow.